Science Advances

AAAS

Supplementary Materials for

Visualizing weakly bound surface Fermi arcs and their correspondence to bulk Weyl fermions

Rajib Batabyal, Noam Morali, Nurit Avraham, Yan Sun, Marcus Schmidt, Claudia Felser, Ady Stern, Binghai Yan, Haim Beidenkopf

This PDF file includes:

- Extended *q*-space map
- *dI/dV* maps: Raw data and symmetrization
- Fermi arc scattering signature
- Agreement between vacancy- and step edge–induced QPI
- Fermi arc dispersion
- Correlation between scatterer-free *dI/dV* modulations and replications of QPI patterns
- Correspondence between QPI patterns and Bloch wave function
- Band structure calculations
- Extracting the intensity of QPI features
- Splitting the line-cut *dI/dV* into submaps
- fig. S1. Extended *q*-space map.
- fig. S2. *dI/dV* maps: Raw data and symmetrization.
- fig. S3. QPI pattern involving Fermi arc scattering from a different vacancy distribution.
- fig. S4. Agreement between vacancy- and step edge–induced QPI.
- fig. S5. Calculated Fermi arc dispersion.
- fig. S6. Structure of the Bloch wave function and its correspondence to QPI.
- fig. S7. Wave function distribution.
- fig. S8. Extraction of QPI feature intensities.
- Reference (*36*)

1. Extended q-space map

To examine whether there are significant replication of QPI features to Bragg peaks higher than the first, we have taken a high resolution dI/dV map (pixel per 0.5Å, corresponding topography in fig. S1a). The q-space field of view we obtain contains 3rd order Bragg peaks. We indeed confirm that replications of QPI features are detected around q=0 and the 1st Bragg peak only (fig. S1b).
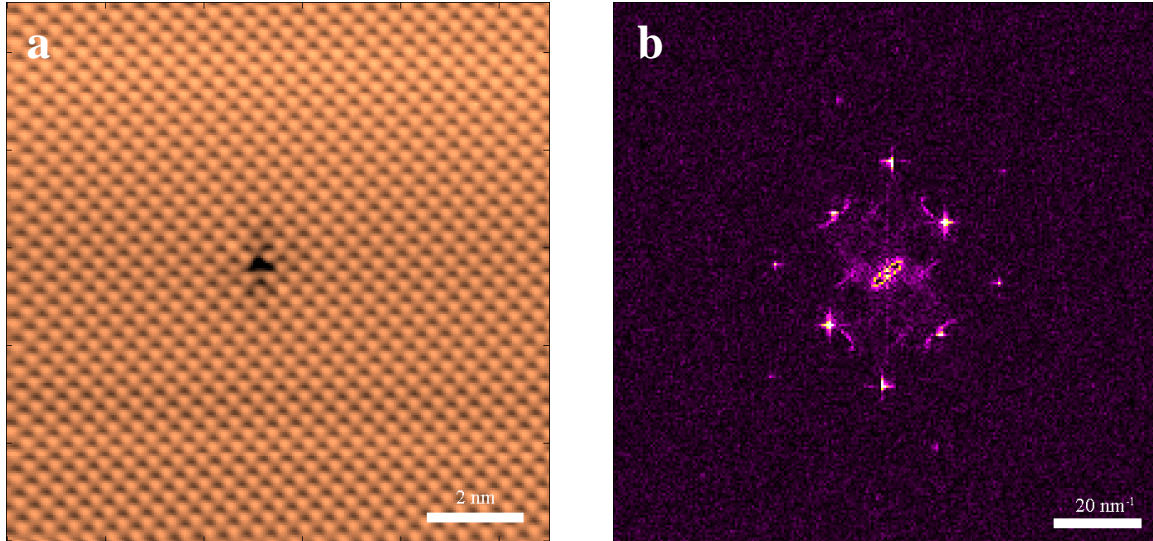

fig. S1. Extended q-space map. (a) Topographic image taken during measurement of a high-resolution dI/dV map (pixel per 0.5 Å). **(b)** Fourier transform of a dI/dV map measured over the region in left panel. No QPI signatures detected around Bragg peaks higher than the 1st order.

2. dI/dV maps: Raw data and symmetrization

We make use of the mirror symmetry of the crystal in order to enhance the signal to noise ratio of the QPI data, in which the mirror symmetry is commonly diminished due to small anisotropies in the rastering mechanism. Figure S2 shows the same map of fig. S1, in other energy values, after mirroring (and rotation). For each data set used we confirm that no features are added or eliminated by the mirroring procedure. We note that a leaf-like pattern about q~0 does not repeat at all energies (e.g., fig. S2II-c,d), as would be the case had it originated from some long-wavelength modulations due to an underlying inhomogeneous potential.
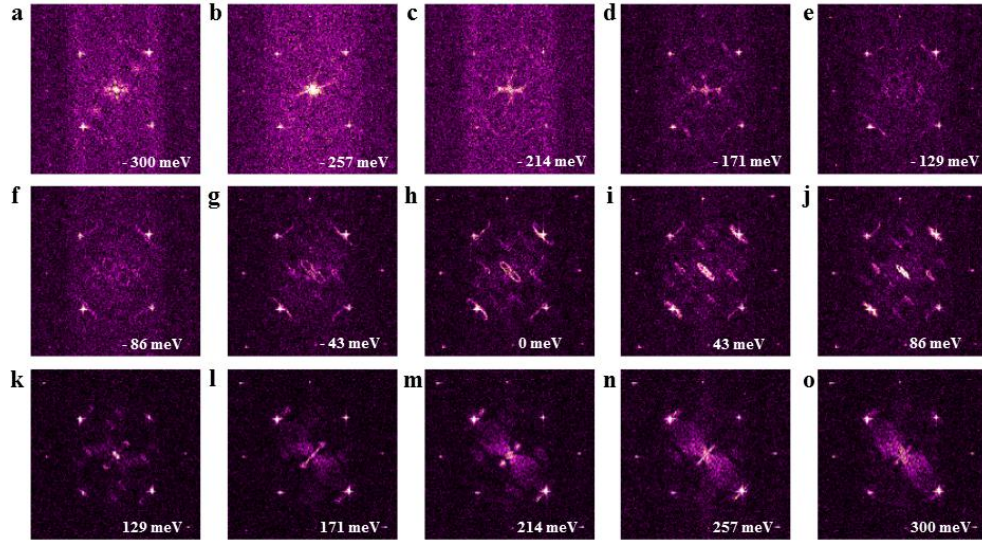
fig. S2I. Raw *dI/dV* maps. (a-o) Raw Fourier transformed *dI/dV* maps at different energies. All features discussed appear in the raw data.
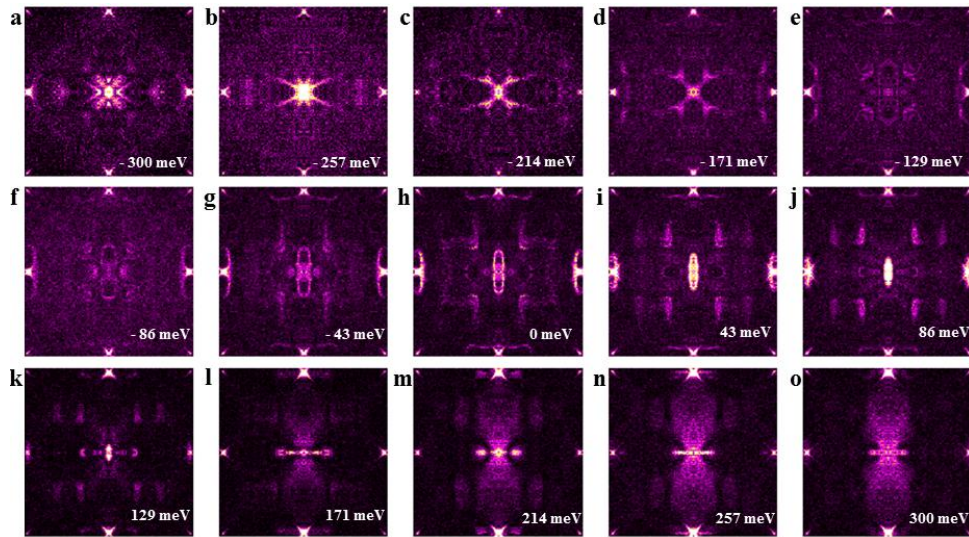

fig. S2II. Mirroring of QPI maps. (a-o) to enhance the symmetric features based on the mirror symmetry of the crystal the raw QPI maps were first rotated to align the Bragg peaks, and mirrored around a mirror axis taken along two opposite Bragg peaks. No features were artificially added or eliminated during this procedure. Mirror symmetry broken mainly by minute anisotropy in the scanning mechanism is restored.

3. Fermi arc scattering signature

An additional data-set taken over a different region (with respect to the one shown in Fig. 1 of the main text) on the surface of the same sample show the leaf-like patterns that we associate with scattering involving Fermi-arcs. This demonstrates that this feature is not due to a specific realization of a vacancy distribution or any other local parameter, but rather a property of the interfering electrons.
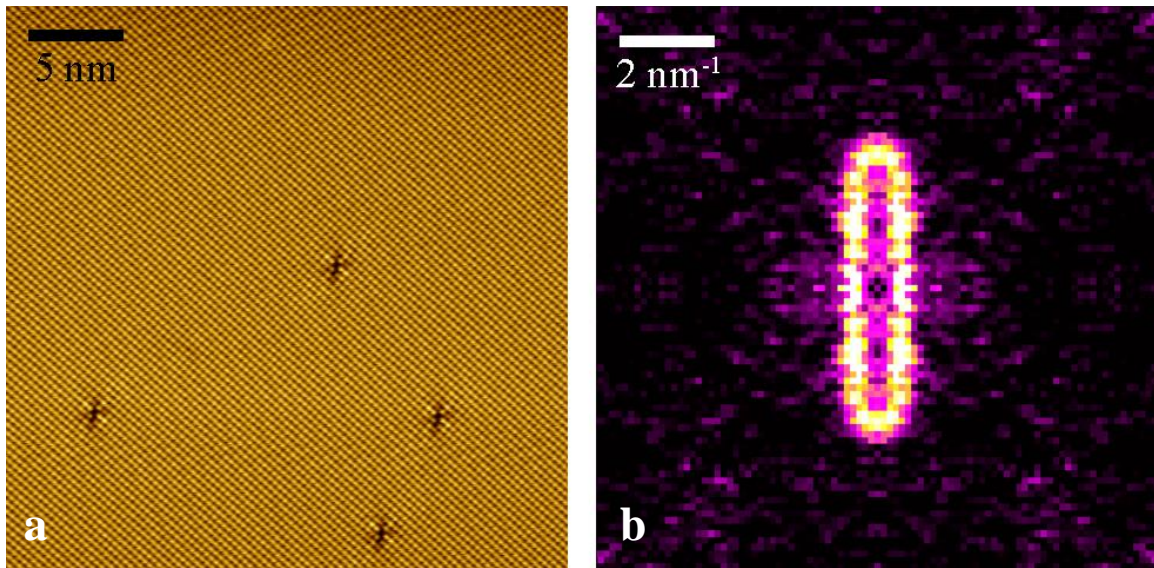

fig. S3. QPI pattern involving Fermi-arc scattering from a different vacancy distribution.
(a) Topographic image showing the local distribution of As vacancies over which the presented *dI/dV* map was taken. **(b)** Fourier transform of that *dI/dV* map showing a leaf-like pattern similar to that of Fig. 1F. Momentum resolution is somewhat lower due to smaller spatial field of view imaged.

4. Agreement between vacancy- and step edge–induced QPI

The step edge that we measure is oriented 49° relative to the Γ-X crystallographic direction (see Fig. 2A). The Fourier transform of the 1D interference pattern that we measure due to scattering off this step edge at the Fermi energy (E_F) perfectly agrees with 2D QPI pattern (along the same cut) that we measure off vacancies at the corresponding energy.
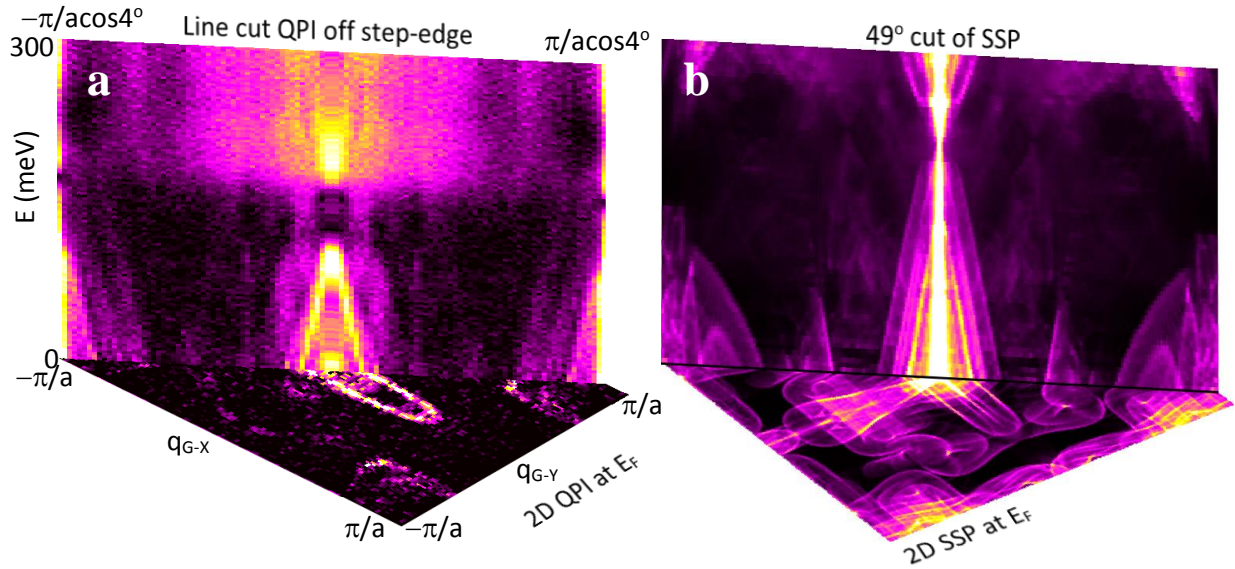
fig. S4. Agreement between vacancy- and step edge–induced QPI. (a) 3D plot presenting the line cut's QPI data in the vertical plane crossing the horizontal 2D vacancy induced QPI map at the right angle (49°) and energy (0meV). It shows the correspondence between the identified features in the 2D QPI pattern – namely, ellipse at q=0 and squares at zone edges – and their dispersion. **(b)** corresponding SSP.

5. Fermi arc dispersion

The extent of the Fermi-arcs in momentum space decreases as the Weyl node is approached. At the energy of W2 the arc locus becomes almost a straight line connecting the pair of nodes. As a result , at the Weyl energy, the shortest q vector in the QPI pattern involving the Fermi arcs results from scattering between k values in the vicinity of the Weyl nodes. As a consequence it represents the distance between the Weyl nodes.
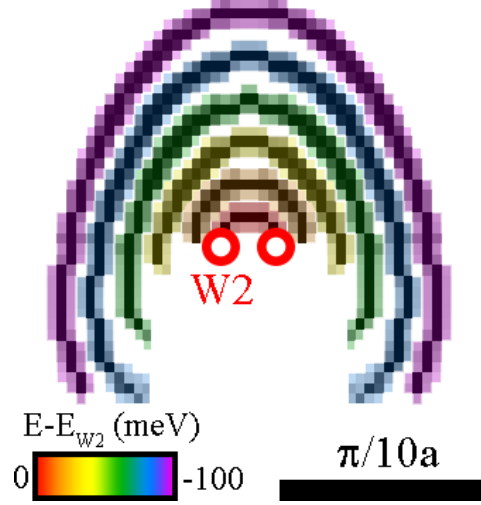
fig. S5. Calculated Fermi arc dispersion. Fermi-arc extent shrinks as the W2 Weyl node's energy (~2meV above Fermi energy) is approached.

6. Correlation between scatterer-free *dI/dV* modulations and replications of QPI patterns

The QPI patterns that we observe near scatterers show clear replications of several patterns around adjacent Bragg peaks, while the spatial maps of local density of states in scatterer-free regions show oscillations on the scale of a unit cell. Both of these phenomena reflect the interaction of the electrons with the periodic lattice potential.

Bloch theorem constrains a state with a crystal momentum k to be a super-position of momenta $k + G$, where G is a vector in the two dimensional reciprocal lattice, $\Psi_k(r) = \sum_G C_G^k e^{i(k+G)\cdot r}$. Consequently, the local density of states $\rho(E, r) = \sum_k |\Psi_k(r)|^2 \delta(E - \epsilon_k)$ in a vacancy-free region becomes $\rho(E, r) = \sum_g A_g e^{ig\cdot r}$ where $A_g = \sum_{G,k} C_G^{*k} C_{G+g}^k \delta(E - \epsilon_k)$ is the amplitude of the Bragg peak that corresponds to $g = G - G'$, the position is denoted by r, the energy by E, and E_k the energy of the state with momentum k. A state with multiple significant coefficients C_G^k is generally a state with a fine structure within the unit cell.

A vacancy violates the periodicity and adds a potential *V(r),* whose Fourier transform is V_q. A realistic Gaussian-like impurity potential with a scale $\lambda < a$ (where a is the lattice constant) would yield a QPI pattern that is gradually attenuated with increasing momentum, with a characteristic decay momentum of $2\pi/\lambda$. While we do not know the details of the potential, it is reasonable to expect that it allows momentum transfer that extends beyond $2\pi/a$. The vacancy may scatter an electron from a state $\Psi_k(r)$ to a state $\Psi_{k'}(r)$ through a series of momentum transfers q_g satisfying $q_g = k - k' + g$. The amplitude for each such process is proportional, within the Born approximation, to $\sum_{G'} V_{q_g} C_{G'+g}^{*k} C_{G'}^{k'}$. Hence, multiple significant coefficients C_G^k result in multiple replicas of the QPI around several Bragg peaks (30), limited by the ability of the potential to provide the required momentum transfer. The QPI pattern at momentum q, which is

the Fourier transform of the local density of states, sums all the scattering processes that involve a momentum q, provided that both E_k and $E_{k'}$ are identical to the energy being probed.

The QPI pattern that we measure for the non-topological states is highly anisotropic in a band selective manner (bowtie strongly replicated in Γ-X, ellipse in Γ-Y), highly dispersive, non-monotonic in q (patterns at Bragg peaks are sometimes more intense than the one at q=0, see Fig. 4A) and sharply changing at high q (note ellipse pattern at Bragg peak half intense, half faint). All these are consistent with the wave functions having several significant Bloch components. The spatial modulations in the scatterer-free regions lend further support to this interpretation. An alternative explanation by which the replicated structure of the QPI emerges from properties of the scattering potential requires an elaborate fine tuning of the potential. As the next subsection shows, the wave function structure that we extract from the QPI pattern is also consistent with the theoretical calculations.

7. Correspondence between QPI patterns and Bloch wave function

From Fig. 4A we conclude that at low energies the bowtie QPI appears in comparable intensities at q=0 and around the Bragg peak. At somewhat higher energies (-70meV <E< 80meV) the Bragg peak pattern dominates, while at yet higher ones the q=0 pattern becomes dominant. The ellipse appears with comparable intensities around these two q values at most energies at which this band exists. We further note that around Bragg peaks both the ellipse and the bowtie appear relatively intense at q<G and fainter at q>G. We have not detected any signature of replications for the Fermi arcs, which probably means their wavefunction contains a single dominant Bloch term, or several components whose momentum difference is larger than the scale of momentum of the potential.

We now demonstrate how the calculated structure of the Bloch wavefunction of the different bands can reproduce these features. We first show in fig. S6 calculated Bloch coefficients of the three bands at energy -100meV and at a single momentum (point 6 in inset). Remarkably, we indeed find that both the ellipse and the bowtie wavefunctions are constructed from two main Bloch terms of adjacent G values. For the ellipse these are $G_{0,0}$ $G_{0,-1}$ (the subscripts refer to the number of reciprocal basis vectors in the x and y directions), while for the bowtie we find $G_{0,0}$ and $G_{-1,0}$. Indeed in the vacancy-free *dI/dV* map we find modulations in the Γ-Y at energies where the ellipse band dominates, and modulation in the Γ-X direction when the bowtie band dominates the *dI/dV* map. In contrast, for the Fermi arc we find a Bloch wavefunction which is strongly dominated by a single term - $G_{0,0}$. Hence, it is never replicated to higher Bragg peaks, and unlike dangling-bond derived trivial bands, it is weakly modulated by the surface potential.
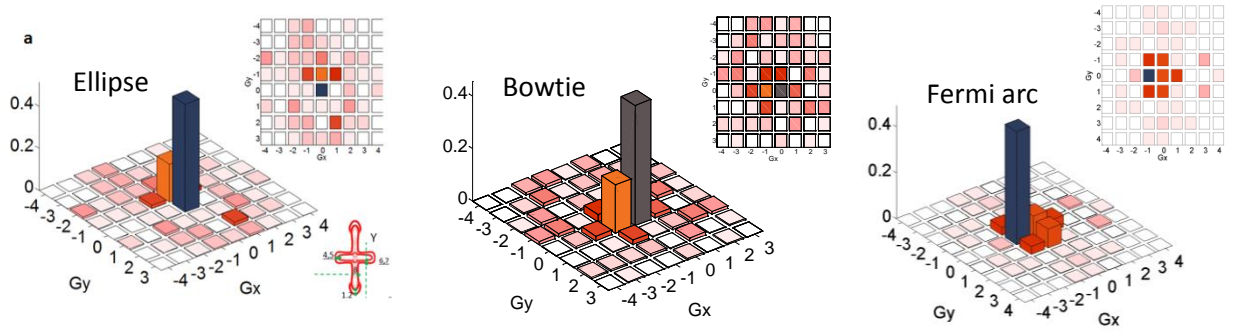
fig. S6I. Structure of the Bloch wave function of the different bands. Coefficients of the Bloch wave function calculated by DFT for the ellipse, bowtie and Fermi arc bands (left to right) at E=-100meV and k marked by points 6,8,1, respectively, at inset. It shows the anisotropy of the Bloch wave function of the ellipse and bowtie bands along Γ-X and Γ-Y respectively as they have dominant G's along these directions in addition to the dominant G=0 terms. In contrast, the Fermi-arc wavefunction is composed of a single dominant G, and several evenly distributed subdominant coefficients reflecting its extended isotropic nature.

From this distribution of coefficients of the ellipse, for instance, one can construct a rough picture of the wave functions in the range of momenta that covers nine Brillouin zones as shown in fig. S6II (left), where color represents the intensity of Bloch coefficient in fig. S6I with matching color (i.e. gray – strong, orange – intermediate, pink – weak but finite). The intensity of the various instances of the QPI pattern can be read off from this information by multiplying the intensities of the initial and final wave numbers. Accordingly the strongest QPI signal originates from scattering between states for which $k_x \approx \pm \left| \frac{\pi}{a} - \delta k \right|$ (with a small δk) and $k_y \approx 0$. This scattering appears around the Γ-Y Bragg peak. Since only the internal halves of the ellipse band have strong Bloch coefficients only half an ellipse will appear strong in that QPI pattern, as indeed seen at the QPI pattern fig. S6II (right). The next dominant QPI pattern would arise from scattering between $k_x \approx \frac{\pi}{a} \pm \delta k$ (with a small δk) and $k_y \approx 0$ (gray to orange) and would generate the slightly weaker QPI pattern at q=0. Next contribution comes from scattering between momenta at the remote zones on either side of the central one (orange to orange) which contributes the faint external halves of the QPI pattern at the Γ-Y Bragg peak. These are hardly seen in the QPI shown in fig. S6II (right), but detected at other energy cuts as in the Fermi energy E_F (Fig. 1C). The faintest ellipse QPI pattern we still track would come from momentum transfer along the y axis, between states where $k_x \approx \frac{\pi}{a} \pm \delta k$ (with a small δk) and $k_y \approx 0$ to states where $k_x \approx \frac{\pi}{a} + \delta k$ (with a small δk) and $k_y \approx \pm \frac{2\pi}{a}$ (gray to red). The QPI signal of this event appears at the Γ-X Bragg peak (barely observed in Fig. 1C). A similar analysis may be carried out for QPI patterns of other bands.
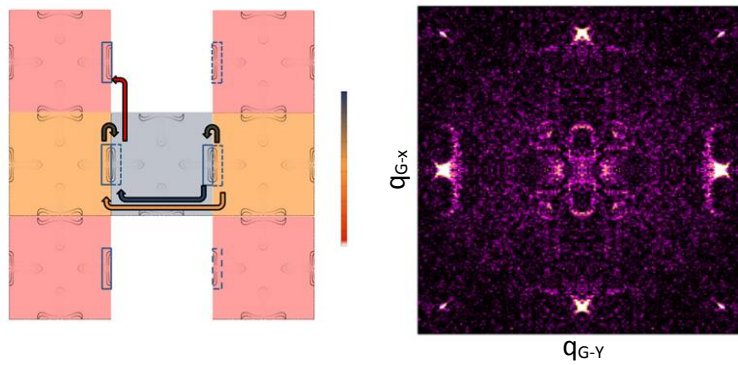
fig. S6II. Correspondence between calculated Bloch wavefunction and the QPI pattern. Left layout of momentum space, centered around zero momentum, where color of the different zones mark the intensity of their associate coefficient in the Bloch wave function of the ellipse band shown in fig. S6I. The intensity of the QPI pattern around a given Bragg peak g=G-G' is correlated with the intensity of the multiplication of the Bloch coefficients of the relevant scattering process $C_{k,G}C^*_{k+G',G'}$. **Right:** QPI pattern at corresponding energy (-100meV). Replications of the ellipse (as well as bowtie) band appear with matching intensities.

8. Band structure calculations

The ab-initio density-functional theory calculations were performed in the generalized-gradient approximation level with spin-orbital coupling, which is implemented in the Vienna *ab initio* simulation package (VASP; *36*). To simulate the surface, a slab model with a thickness of seven unit cells was constructed, in which the top and bottom surface are terminated by As and Ta, respectively. The surface band structures and the Fermi surface were projected to the first unit cell of the As-terminated side, which fits the previous experimental band structure well (*13*).
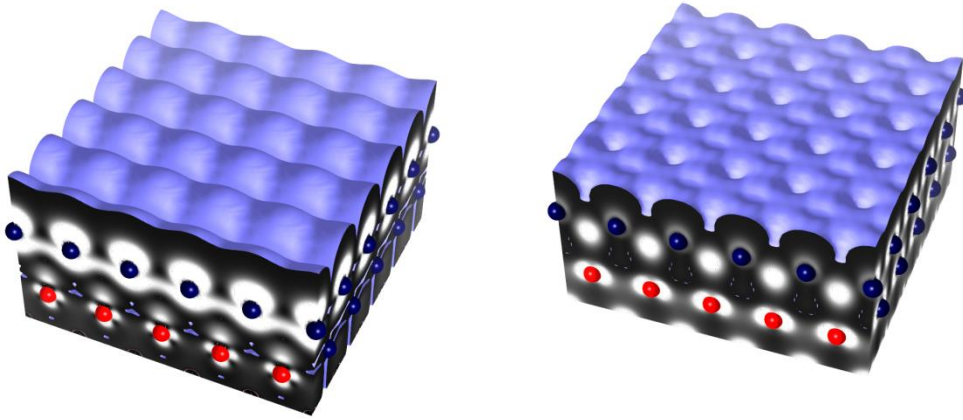
fig. S7. Wavefunction distribution. Ab-initio calculation of the wavefunction equal density surface calculated for the ellipse band (left) and Fermi arc (right) at -100meV and arbitrary k-value. The Fermi arc's density profile is smoother and isotropic compared to the elipse's distribution.

9. Extracting the intensity of QPI features

In Fig. 4A we plot the average intensity across the ellipse and bowtie around q=0 and Bragg peaks. To extract these intensities we have manually defined the maximal bounding box around a quarter of each feature such that will not contain neighboring features. We then averaged over the 30 highest maxima within the bounding box making sure that these maxima indeed fall on the feature of interest and not on a spurious high intensity pixel. From this value we have subtracted the average background in the vicinity of the box (note that the background level is more than an order of magnitude weaker than the intensity of the features, and therefore had little effect on the resulting value). We have repeated this procedure around the Bragg peak by translating the bounding box by a reciprocal wave vector such that the bounding box is defined once per feature.

For the subtraction of the Bragg peak QPI from the q=0 one we have constructed the multiple zone boundaries based on the atomic Bragg peaks, and subtracted the average of two zones centered about opposite Bragg peaks, normalized to the average intensity of the feature to be eliminated in the central q=0 zone.
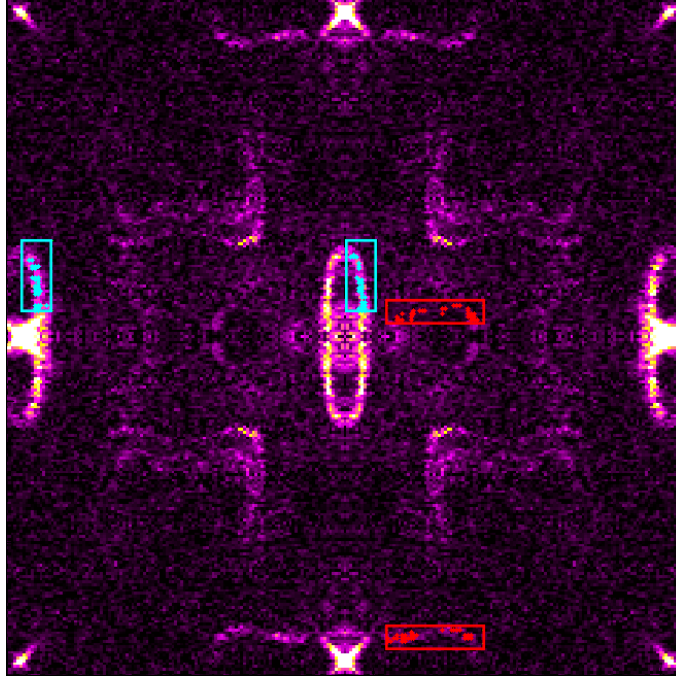
fig. S8. Extraction of QPI feature intensities. We average over 30 pixels of maximal intensity within a predefined bounding box

10. Splitting the line-cut *dI/dV* into submaps

In Fig. 2 we split the measured *dI/dV* line-cut map (Fig. 2B) into two separate submaps, one contains the *dI/dV* features measured on As sites (Fig. 2E) and the other on Ta (Fig. 2F). Figure 2B already shows the *dI/dV* after the DC term has been removed (by subtracting the average *dI/dV* value at each energy). As a result false color shows position with intensity larger than the average (blue) and smaller (red). We find perfect correlation between the atomic sites in the topographic profile displayed at the bottom and the large/small intensity pattern. Accordingly the sign of the flattened *dI/dV* corresponds to being on/off atomic sites. We then split this map gathering locations with low and high intensities separately, which forms Fig. 2E,F. Since the distribution of these points is regular this amounts to lowering the sampling resolution for each submap. The lower spatial resolution results in smaller field of view in *q*-space. However, it allows to separate overlapping low-q features into those residing on/off As sites. Note, that the sum of the Fourier-transformed submaps (Fig. 2G,H) does not yield that of the complete map since the relative phase information is lost when displaying the magnitude of the Fourier decomposition.